

# Fine-Grained Spatiotemporal Motion Alignment for Contrastive Video Representation Learning

Minghao Zhu  
tjdezmh@tongji.edu.cn  
Tongji University

Xiao Lin  
2111118@tongji.edu.cn  
Tongji University

Ronghao Dang  
dangronghao@tongji.edu.cn  
Tongji University

Chengju Liu\*  
liuchengju@tongji.edu.cn  
Tongji University

Qijun Chen  
qjchen@tongji.edu.cn  
Tongji University

## ABSTRACT

As the most essential property in a video, motion information is critical to a robust and generalized video representation. To inject motion dynamics, recent works have adopted frame difference as the source of motion information in video contrastive learning, considering the trade-off between quality and cost. However, existing works align motion features at the instance level, which suffers from spatial and temporal weak alignment across modalities. In this paper, we present a **Fine-grained Motion Alignment (FIMA)** framework, capable of introducing well-aligned and significant motion information. Specifically, we first develop a dense contrastive learning framework in the spatiotemporal domain to generate pixel-level motion supervision. Then, we design a motion decoder and a foreground sampling strategy to eliminate the weak alignments in terms of time and space. Moreover, a frame-level motion contrastive loss is presented to improve the temporal diversity of the motion features. Extensive experiments demonstrate that the representations learned by FIMA possess great motion-awareness capabilities and achieve state-of-the-art or competitive results on downstream tasks across UCF101, HMDB51, and Diving48 datasets. Code is available at <https://github.com/ZMHH-H/FIMA>.

## CCS CONCEPTS

• **Computing methodologies** → **Activity recognition and understanding**; **Unsupervised learning**.

## KEYWORDS

Self-supervised Learning; Action Recognition

## ACM Reference Format:

Minghao Zhu, Xiao Lin, Ronghao Dang, Chengju Liu, and Qijun Chen. 2023. Fine-Grained Spatiotemporal Motion Alignment for Contrastive Video Representation Learning. In *Proceedings of the 31st ACM International Conference*

\*Corresponding author.

Permission to make digital or hard copies of all or part of this work for personal or classroom use is granted without fee provided that copies are not made or distributed for profit or commercial advantage and that copies bear this notice and the full citation on the first page. Copyrights for components of this work owned by others than the author(s) must be honored. Abstracting with credit is permitted. To copy otherwise, or republish, to post on servers or to redistribute to lists, requires prior specific permission and/or a fee. Request permissions from [permissions.acm.org](https://permissions.acm.org).

MM '23, October 29–November 3, 2023, Ottawa, ON, Canada.

© 2023 Copyright held by the owner/author(s). Publication rights licensed to ACM.

ACM ISBN 979-8-4007-0108-5/23/10...\$15.00

<https://doi.org/10.1145/3581783.3611932>

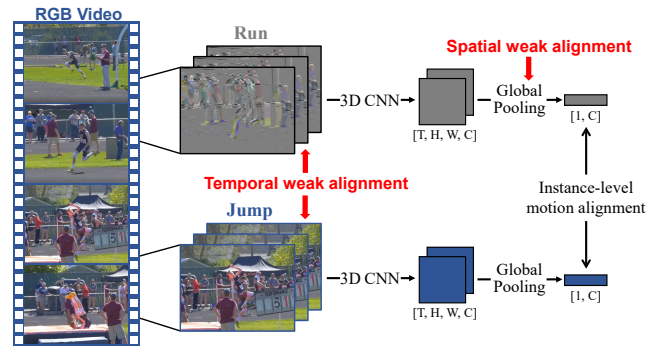


**Figure 1: An illustration of weak alignment across modalities. For temporal weak alignment, since motion semantics varies over time, direct alignment of features with different timestamps introduces minimal shared information. For spatial weak alignment, the pooled feature is distracted by cluttered background noise, leading to misalignment of background features and inadequate alignment of foreground features.**

on *Multimedia (MM '23)*, October 29–November 3, 2023, Ottawa, ON, Canada. ACM, New York, NY, USA, 14 pages. <https://doi.org/10.1145/3581783.3611932>

## 1 INTRODUCTION

With the enormous growth of uncurated data on the Internet, self-supervised learning came with the promise of learning powerful representations from unlabelled data that can be transferred to various downstream tasks. In particular, contrastive self-supervised learning based on instance discrimination [61] has achieved great success in both NLP [7, 13] and computer vision [10, 23, 46]. In the video domain, this learning diagram has also presented promising performance by keeping the instances within the same video semantically consistent [16, 45]. However, vanilla video contrastive learning has difficulty modeling local temporal information [12, 43] and possesses severe background bias [14, 55], which limits the generalization and transferability of the learned representations. The reason may stem from the existence of static bias in the positive pair construction. The features of temporally separated instances could be easily pulled close by attending to the static cues while neglecting the dynamic details, which provide crucial information for discrimination and downstream tasks.

To alleviate the background bias in the context of contrastive learning, an effective method is to introduce motion information.

Previous works incorporate motion information either by constructing motion-prominent positive pairs via meticulously designed data augmentations [14, 54, 55] or using other modalities to explicitly enhance motion information in feature space [33, 39, 62]. Among them, aligning the motion features of optical flow in an explicit way achieves impressive results. But the expensive computation cost limits the scalability of optical flow on large-scale datasets. Hence, how to incorporate motion information effectively without resorting to costly accessories has attracted a lot of attention.

Frame difference, an alternative with a negligible cost for optical flow, can extract motion across frames by removing the still background. But its quality is extremely susceptible to background noise caused by camera jitter or drastic changes in the background. Several approaches [15, 43, 49, 50] employ it in video contrastive learning and show promising results. Even with notable improvements in performance, how to effectively align the RGB and frame difference features in the latent space still not be fully explored.

The previous works align the features of RGB and frame difference from temporally different views by using global feature vectors [15, 50], which may suffer from the *weak alignment* between the two modalities. As illustrated in Fig. 1, we summarize and categorize the weak alignment problem into two types: temporal weak alignment and spatial weak alignment. Temporal weak alignment signifies that two clips at different timestamps are not semantically consistent in the concept of motion. Some action classes consist of multiple stages of sub-motions. For example, high jumping in Fig. 1 has two motion stages: running and jumping. These two stages have very different motion semantics, and directly pulling them close in the feature space will make the model invariant to the motion semantic changes along the temporal dimension. Spatial weak alignment can be viewed as an inherent problem of the instance-level contrastive learning framework. The global average pooling extends the receptive field of the features to the entire view and compresses all information into a one-dimensional vector, resulting in the pooled features losing spatial information and being distracted by background noise. Simply aligning the pooled features may lead to the misalignment of background features and inadequate alignment of foreground features. As shown in Fig. 1, since the frame difference contains a lot of background noise, the alignment of pooled features becomes sub-optimal for introducing significant motion information.

In this paper, we present a novel framework to introduce well-aligned motion features in video contrastive learning, namely **Fine-grained Motion Alignment (FIMA)**. We argue that the alignment of motion features should be at a more fine-grained level. To this end, we discard the global average pooling and construct a pixel-level contrastive learning framework, where each pixel of the RGB feature map tries to predict the motion feature pixels at the same spatial location but the different timestamps. In this way, the alignments of foreground and background features are sufficient and decoupled. Based on it, we address the temporal weak alignment by designing a motion decoder that takes the RGB feature map from the target view as the bridge between temporally distant positive pairs. This task requires the model to not only learn the correct correspondence between RGB features from the target and the source view but also encode enough motion information for cross-modality reconstruction. Thus, spatiotemporally discriminative motion features can

be learned. To tackle the spatial weak alignment, we propose a foreground sampling strategy to filter out the background pixels in the construction of positive pairs, hence avoiding the distraction of background noise. In addition, we further propose a frame-level motion reconstruction task for improving the temporal diversity of the motion features. Given a frame of RGB feature map, the motion decoder learns to reconstruct the exactly overlapped local motion feature and distinguish it from others. We summarize our main contributions as follows:

- We demonstrate the weak alignment problem between RGB and frame difference modalities, and analyze the influence of the weak alignment in terms of time and space.
- We present a novel FIMA framework, consisting of a dense contrastive learning paradigm, a foreground sampling strategy, and a motion decoder to eliminate the weak alignment of two modalities at the pixel and the frame level, which enhances the self-supervised representations.
- Our framework achieves state-of-the-art or competitive results on two downstream tasks, action recognition, and video retrieval, across UCF-101, HMDB-51, and Diving-48 datasets.

## 2 RELATED WORK

**Self-supervised learning in videos.** Self-supervised learning aims to learn transferable representations from large-scale unlabeled data. In the video domain, early works focus on encoding intrinsic structure information by solving sophisticated designed pretext tasks, including temporal transformation [5, 26, 38, 60, 65, 66], statistics prediction [17, 56], and spatiotemporal puzzles [29, 35]. Later, contrastive learning based on instance discrimination [61] makes great progress in the image domain [10, 19, 23]. Some works extend it into video representation learning and achieve promising results [16, 45]. To further enhance video representations, a line of works construct various positive views by applying spatiotemporal augmentations [4, 14, 31, 41, 44]. Besides, [9, 24, 68] formulate predictive tasks in a contrastive manner. [1, 28] leverage the idea of clustering in video contrastive learning. [1, 37, 47] seek consistency between multi-model data, such as audio, text, and optical flow.

**Alleviation of background bias in videos.** Background bias in commonly used datasets may lead to the model over-focusing on static cues, resulting in poor generalization. To overcome this, [34] proposes a procedure to assemble a less biased dataset. In the context of video self-supervised learning, DSM [54], BE [55], and FAME [14] implicitly mitigate the background bias by constructing motion-prominent positive or negative samples. [33, 39, 62] explicitly introduce motion information into feature space from other modalities like optical flow. DCLR [15] uses frame difference as motion supervision and decouples it from data input and feature space. In this paper, we address the background bias by selectively introducing significant motion information from frame difference.

**Dense supervision in contrastive learning.** Dense contrastive learning is initially devised for dense prediction tasks in the image domain [59, 64], such as object detection and semantic segmentation. It preserves spatial information by constructing pixel-level positive pairs between dense features from different views. In the video domain, some works exploit dense supervision in contrastive learning. [21, 22, 25] propose to predict dense feature maps in the

future. They generate positive samples by applying consistent geometric transformation across a video. However, such a strategy can not induce sufficient occlusion invariance, which has been proven to be crucial for contrastive representation learning [42]. [67] extends [59] to the video domain and constructs region-level positive pairs by calculating the correspondence between local RGB features. But this strategy hardly establishes a correct correspondence between RGB and frame difference due to the discrepancy between the two modalities. To address these limitations, our method extends [64] to the spatiotemporal domain and constructs positive pairs based on spatial location prior.

### 3 METHOD

An overview of our proposed framework is presented in Fig. 2. In Section 3.1, we first revisit vanilla spatiotemporal contrastive learning and extend it to the pixel level to generate dense motion supervision. In Section 3.2, we elaborate on the motion decoder and foreground sampling strategy designed to eliminate temporal and spatial weak alignment. Finally, we present the frame-level motion reconstruction task to improve the feature diversity in Section 3.3.

#### 3.1 Pixel-level Contrastive Learning in Videos

Given a video, the vanilla instance-level spatiotemporal contrastive learning randomly samples two video clips  $\{V, \tilde{V}\}$  at different timestamps. The clips are augmented by temporally consistent augmentation [45] and processed by a feature encoder with the global average pooling to extract corresponding video-level representations  $\{v, \tilde{v}\}$ . The prevalent InfoNCE loss [40] is adopted for optimization:

$$\mathcal{L}_{VV} = -\log \frac{h(v^q, \tilde{v}^k)}{h(v^q, \tilde{v}^k) + \sum_{\tilde{v}^k} h(v^q, \tilde{v}^k)}, \quad (1)$$

where  $h(x, y) = \exp(g(x)^T g(y) / \|g(x)\| \|g(y)\| \tau)$  measures the similarity between two projected feature vectors  $g(x)$  and  $g(y)$ ;  $g(\cdot)$  is a non-linear projection head network;  $\tau$  is the temperature parameter; Negative keys  $\tilde{v}^k$  are taken from a memory bank as we follow the network design of MoCo [23]. Note that the superscripts  $q$  and  $k$  indicate the features extracted by the query encoder and the momentum encoder, respectively. This training objective aims to pull the query and its positive key closer while it repels other negative keys in the latent space. However, the representations learned based on Eq. (1) are easily overwhelmed by static background cues [14, 55] and lack the ability to capture dynamic motion information [12]. To introduce motion information, previous works [15, 50] use frame difference as the other motion representation learning branch. We calculate the frame difference  $\tilde{D}$  by differentiating adjacent frames of  $\tilde{V}$  and extract the motion feature  $\tilde{d}^k$ . The motion contrastive loss is as follows:

$$\mathcal{L}_{VD} = -\log \frac{h(v^q, \tilde{d}^k)}{h(v^q, \tilde{d}^k) + \sum_{\tilde{d}^k} h(v^q, \tilde{d}^k)}, \quad (2)$$

where  $\tilde{d}^k$  is the motion features of other videos in a memory bank.

As mentioned in Section 1, the globally average-pooled features cannot be well-aligned due to the weak alignment between modalities. Thus, we extend the dense contrastive learning framework [64] to the spatiotemporal domain to generate dense motion supervision. The representations extracted from  $\{V, \tilde{D}\}$  are kept as feature

maps, denoted as  $\{F^q, \tilde{M}^k\} \in \mathbb{R}^{T \times H \times W \times C}$ , where  $T, H, W, C$  are the dimensions of the time, height, width, channel, respectively.  $F_i^q$  and  $\tilde{M}_i^k$  represent the  $i$ -th frame of the feature maps. For each feature pixel  $f_i^q \in F_i^q$ , we assign a positive pixel set  $\phi_p^k \subseteq \tilde{M}_i^k$  based on the spatial location prior. Specifically, we record the original coordinates of the clip when applying the geometric transformation (e.g. crop and flip). Then, each feature pixel in  $F_i^q$  and  $\tilde{M}_i^k$  is warped to the original video spatial space, and the two-dimensional (height and width) Euclidean distances between  $f_i^q$  and all pixels in  $\tilde{M}_i^k$  are computed. The distances are normalized to the diagonal length of a feature map bin and a hyperparameter  $\mathcal{T}$  is used to measure the distance in scale. We set the threshold  $\mathcal{T} = 0.7$  by default. The pixels in  $\tilde{M}_i^k$  with a distance smaller than  $\mathcal{T}$  are assigned to the  $\phi_p^k$ . The rest of the pixels in the feature map  $\tilde{M}^k$  and motion feature pixels from other videos are assigned to negative pixel set  $\phi_n^k$ . The pixel-level motion contrastive loss can be formulated as:

$$\mathcal{L}_{\text{Pix}} = -\log \frac{\sum_{\tilde{m}_i^k \in \phi_p^k} h(f_i^q, \tilde{m}_i^k)}{\sum_{\tilde{m}_i^k \in \phi_p^k} h(f_i^q, \tilde{m}_i^k) + \sum_{\tilde{m}_i^k \in \phi_n^k} h(f_i^q, \tilde{m}_i^k)}. \quad (3)$$

Note that the projection head  $g(\cdot)$  here is instantiated as two successive  $1 \times 1$  convolution layers to adapt the input form of the feature map. The loss is averaged over all feature pixels in  $F^q$  with at least one positive pair (i.e., corresponding  $\phi_p^k \neq \emptyset$ ). Intuitively, given an RGB feature pixel in the source view, the network learns to predict the motion features at the same spatial location in the target view.

#### 3.2 Fine-grained Motion Feature Alignment

The pixel-level  $\mathcal{L}_{\text{Pix}}$  constructs a framework for fully utilizing dense motion supervision. Based on it, we propose to separately eliminate the weak alignment of motion features in terms of time and space. **Temporal Weak Alignment Elimination.** The positive pair constructed by  $\mathcal{L}_{\text{Pix}}$  still exists two limitations: the first is that the loss pulls features at different timestamps close, resulting in the model becoming invariant to the motion semantic change along the temporal dimension; the second is that the receptive field of a feature pixel only covers a limited region, which may lead to a greater semantic discrepancy between positive pairs.

To address these limitations, we propose to use the RGB features  $\tilde{F}^q$  extracted from the target view  $\tilde{V}$  by the query encoder as the bridge between  $F^q$  and  $\tilde{M}^k$ . To this end, we design a motion decoder based on the attention mechanism, which is quite effective in spatiotemporal dependence modeling [2, 6, 58, 67]. Specifically, we consider the dense features  $\tilde{F}_i^q$  as a collection containing various information. For each RGB feature pixel  $f_i^q \in F_i^q$ , the motion decoder tries to reconstruct the motion features at the same spatial location in the target view by querying the information in collection  $\tilde{F}_i^q$ . Then the pixel-level motion contrastive loss becomes:

$$y_i^q = \text{MD}(f_i^q, \tilde{F}_i^q, \tilde{F}_i^q), \quad (4)$$

$$\mathcal{L}_{\text{Pix}} = -\log \frac{\sum_{\tilde{m}_i^k \in \phi_p^k} h(y_i^q, \tilde{m}_i^k)}{\sum_{\tilde{m}_i^k \in \phi_p^k} h(y_i^q, \tilde{m}_i^k) + \sum_{\tilde{m}_i^k \in \phi_n^k} h(y_i^q, \tilde{m}_i^k)}, \quad (5)$$

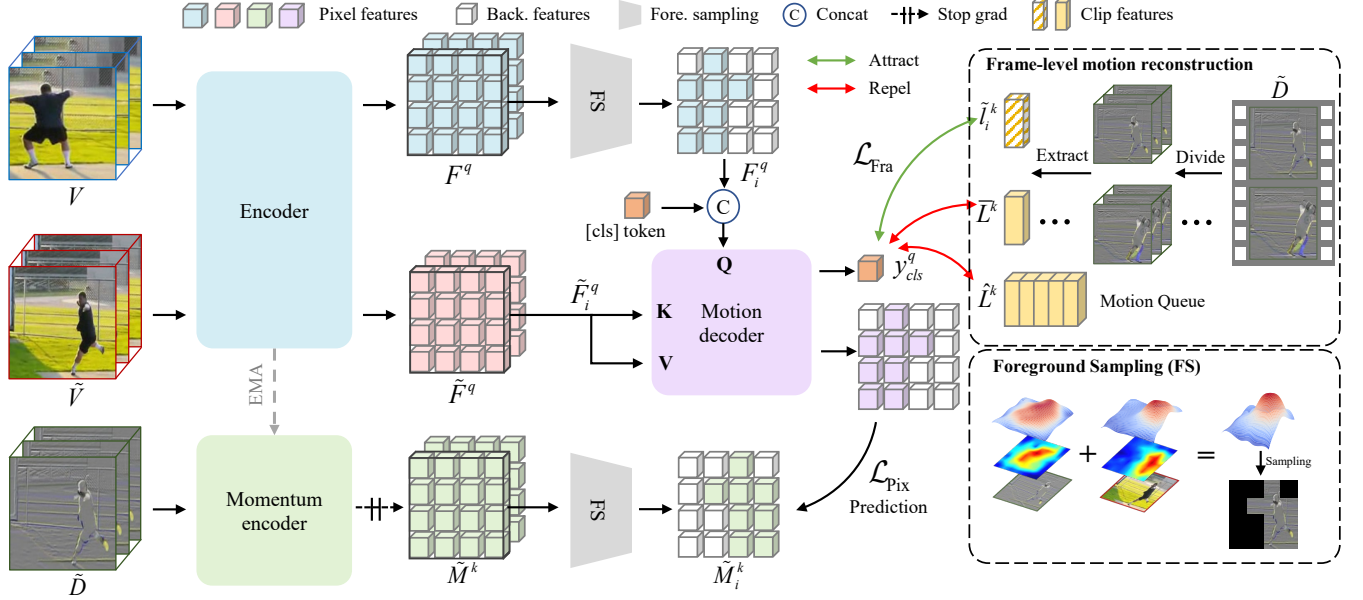


**Figure 2: Overview of the framework.** We sample two temporally distant clips  $\{V, \tilde{V}\}$  and compute the frame difference  $\tilde{D}$ . The corresponding dense feature maps  $\{F^q, \tilde{F}^q, \tilde{M}^k\}$  are extracted by the encoder or its momentum version. We sample the foreground features at the  $i$ -th frame of  $F^q$  and concatenate them with a class token, then feed them into the motion decoder. We use the motion decoder to reconstruct the foreground features of  $\tilde{M}^k$  in the  $i$ -th frame, by collecting information from  $\tilde{F}_i^q$ . Finally, the class token is used to reconstruct the local motion feature with time interval overlaps exactly with  $\tilde{F}_i^q$ .

where  $\text{MD}(Q, K, V)$  refers to the motion decoder implemented by the standard transformer layer [53];  $Q \in \mathbb{R}^{1 \times d}$  is the query feature;  $K, V \in \mathbb{R}^{HW \times d}$  are key-value pairs;  $d$  is the query/key dimension;  $y_i^q$  is the output of the motion decoder. The motion decoder builds the correct correspondence between the RGB features of the source view  $F_i^q$  and the target view  $\tilde{F}_i^q$  and avoids enforcing the features at different timestamps to be similar. It also requires every RGB feature pixel in  $\tilde{F}_i^q$  to encode more motion information around itself for cross-modality reconstruction. Further, the attention operation extends the receptive field of the predicted feature pixels to the entire target view, thus eliminating the semantic discrepancy.

**Spatial Weak Alignment Elimination.** With the proposed dense contrastive learning framework, the alignment of each foreground and background feature pixel is decoupled. We can avoid the disturbance of noise by filtering out the background pixels. As a common visualization technique, class activation maps [3, 69] provide an intuitive way to localize the discriminative regions, by which we expect to classify the foreground and background pixels. However, we find that activation maps from either RGB or frame-difference features easily attend to the incorrect background area. The other observation is that the distribution of the activation map is relatively flat when the model’s attention is disturbed by background noise. In other words, it tends to cover a larger range of the background with lower activation values. Instead, the distribution of the activation map is steeper when the model correctly captures the foreground information. The underlying reason lies in the foreground information being more structural and concentrated, producing a distinct and dense activation region. Based on this observation, we propose

to use the features of two modalities with complementary information to jointly determine the foreground region. Concretely, we compute class-agnostic activation maps [3] of two modalities by applying the average pooling along channel and time dimensions, then fuse them by simple point-wise addition. We divide pixels in the target view  $\tilde{M}^k$  into two mutually exclusive sets  $\tilde{M}_{fg}^k$  and  $\tilde{M}_{bg}^k$  based on the fused activation map  $\tilde{Z}^k \in \mathbb{R}^{H \times W}$  as follows:

$$A(\tilde{m}_{i,j}^k) = \begin{cases} 1, & \text{if } \tilde{z}_j > \beta\text{-th quantile of } \tilde{Z}^k, \\ 0, & \text{otherwise,} \end{cases} \quad (6)$$

where  $\tilde{m}_{i,j}^k$  is a pixel in the feature map  $\tilde{M}^k$ ;  $i$  denotes the temporal index and  $j \in \{(1, 1), (1, 2), \dots, (H, W)\}$  is the spatial index;  $\tilde{z}_j$  is the pixel at spatial index  $j$  in the fused activation map;  $\beta \in [0, 1]$  is a hyper-parameter used to describe the portion of the foreground. We set  $\beta = 0.5$  by default. Similarly, we obtain the foreground set  $F_{fg}^q$  and the background set  $F_{bg}^q$  of the source view  $F^q$  in the same manner. We only sample positive pairs in the foreground regions and the pixel-level motion contrastive loss becomes:

$$y_i^q = \text{MD}(F_i^q, \tilde{F}_i^q, \tilde{F}_i^q), \quad (7)$$

$$\mathcal{L}_{\text{Pix}} = -\log \frac{\sum_{\tilde{m}_i^k \in \phi_p^k \cap \tilde{M}_{fg}^k} h(y_i^q, \tilde{m}_i^k)}{\sum_{\tilde{m}_i^k \in \phi_p^k \cap \tilde{M}_{fg}^k} h(y_i^q, \tilde{m}_i^k) + \sum_{\tilde{m}_i^k \in \phi_n^k} h(y_i^q, \tilde{m}_i^k)}, \quad (8)$$

where  $\phi_n^k$  here indicates the rest of the pixels in the feature map  $\tilde{M}^k$  except  $\{\phi_p^k \cap \tilde{M}_{fg}^k\}$ , plus motion feature pixels from other videos.

**Table 1: Ablation study on the loss designs.**

Contrastive Losses				Linear		Finetune	
$\mathcal{L}_{VV}$	$\mathcal{L}_{Pix}$	$\mathcal{L}_{Fra}$	$\mathcal{L}_{VD}$	UCF101	HMDB51	UCF101	HMDB51
✓				58.1	26.7	76.7	48.8
✓			✓	68.7	37.7	80.8	53.3
✓	✓			73.1	39.2	83.1	54.2
✓		✓		69.7	38.5	81.3	54.1
✓	✓	✓		<b>75.3</b>	<b>42.8</b>	<b>84.2</b>	<b>57.8</b>

The loss is averaged over all feature pixels in the foreground set  $F_{fg}^q$  with at least one positive pair.

### 3.3 Frame-level Motion Feature Reconstruction

The  $\mathcal{L}_{Pix}$  aligns the motion features at the pixel level. To further enhance the temporal diversity of the learned features, we propose a frame-level local motion reconstruction task. We divide the motion clip  $\tilde{D}$  into  $T$  sub-clips, where  $T$  is the time dimension of the corresponding feature map  $\tilde{M}^k$ . Given a frame of the feature map  $\tilde{F}_i^q$ , the motion decoder aims to reconstruct the feature of the sub-clip with time interval overlaps exactly with  $\tilde{F}_i^q$ .

Before input to the motion decoder, we prepend a learnable [cls] token to the sequence of features. For the output state of the class token  $y_{cls}^q$  and the corresponding local motion feature  $\tilde{l}_i^k$ , the frame-level motion contrastive loss can be formulated as:

$$y_{cls}^q = \text{MD}([\text{cls}], \tilde{F}_i^q, \tilde{F}_i^q), \quad (9)$$

$$\mathcal{L}_{Fra} = -\log \frac{h(y_{cls}^q, \tilde{l}_i^k)}{h(y_{cls}^q, \tilde{l}_i^k) + \sum_{l^k \in \{\tilde{L}^k, \hat{L}^k\}} h(y_{cls}^q, l^k)}, \quad (10)$$

where  $\tilde{L}^k$  and  $\hat{L}^k$  are the sets of local features in the same video and other videos. We use the motion decoder shared with  $\mathcal{L}_{Pix}$  to avoid introducing extra overhead. By discriminating the positive from the intra-video negatives and inter-video negatives, the features extracted by the encoder become more temporally discriminative.

The overall learning objective can be written as:

$$\mathcal{L} = \mathcal{L}_{VV} + \mathcal{L}_{Pix} + \mathcal{L}_{Fra}, \quad (11)$$

where we jointly optimize all losses and treat each term equally.

## 4 EXPERIMENTS

### 4.1 Implementation Details

**Datasets.** We conduct experiments on four standard video datasets, UCF101 [48], HMDB51 [32], Kinetics-400 [27], and Diving-48 [34]. We use the updated V2 version of Diving-48 for evaluation.

**Technical Details.** We choose two widely used backbones, R(2+1)D-18 [51], and I3D-22 [8] as the video encoder. The non-linear projection head is instantiated as two successive  $1 \times 1$  convolution layers with an output dimension of 128 to adapt the input form of the feature map. We closely follow the network design of MoCo-v2 [11]. Besides, the negative set  $\phi_n^k$  in  $\mathcal{L}_{Pix}$  is implemented as a queue with a size of 784 for UCF101 and 31360 for Kinetics-400. We show more details in the supplementary material.

**Table 2: Ablation study on the components in  $\mathcal{L}_{Pix}$ . Including dense contrastive learning framework (DC), foreground sampling strategy (FS), and motion decoder (MD). The first line indicates  $\mathcal{L}_{Pix}$  degrades to  $\mathcal{L}_{VD}$ .**

Components			Finetune	Linear
DC	FS	MD		
-	-	-	80.8	68.7
✓			79.7	69.7
✓	✓		81.3	71.2
✓		✓	82.3	71.0
✓	✓	✓	<b>83.1</b>	<b>73.1</b>

We implement the motion decoder by using the standard transformer layer in [53]. As the default setting we use a 2-layer 512-wide model with 4 attention heads. The class token is a learnable 512-dim embedding. A linear layer is attached on two sides to adjust the feature dimension. The motion decoder is placed before the non-linear projection head. We add 1D absolute positional encodings to each feature frame before inputting it into the motion decoder.

**Self-supervised Pre-training.** In the pre-training phase, we randomly sample two 16-frame clips with a temporal stride of 2 at different timestamps and compute the frame difference. Each clip is randomly cropped and resized to the size of  $224 \times 224$  or  $112 \times 112$  and then undergoes random horizontal flip, color jittering, random grayscale, and Gaussian blur in a temporally consistent way [45]. We pretrain the model for 200 epochs on UCF101 or 100 epochs on Kinetics-400. Following the linear scaling rule of the learning rate [18], we set the initial learning rate to 0.00375 with a total batch size of 24 for UCF101 or 0.01 with a total batch size of 64 for Kinetics-400. A half-period cosine schedule is used for the learning rate decay. We adopt SGD as the optimizer with a momentum of 0.9 and a weight decay of  $10^{-4}$ .

**Downstream Task Evaluations.** We evaluate the self-supervised representations on two downstream tasks: action recognition and video retrieval. Following the common practice [12, 22], we average the predictions of 10 uniformly sampled clips of a video as the final result. For action recognition, we use the weights of the pre-trained network as initialization and evaluate the representations under linear probing and fine-tuning settings. We report the top-1 classification accuracy on split 1 of UCF101 and HMDB51, and the v2 test set of Diving-48. For video retrieval, we directly use the pre-trained model as a feature extractor without further training. Following [65], we extract the feature of each video in the test set as a query and retrieve the k-nearest neighbors in the training set by calculating the cosine similarity. We report the top-k recall R@k on UCF101 and HMDB51.

### 4.2 Ablation Study

In this subsection, we perform in-depth ablation studies of FIMA. We pre-trained on split 1 of UCF101 with I3D for 200 epochs. Unless otherwise specified, we report the linear probing and fine-tuning Top-1 classification accuracy on UCF101 split 1.

**Overall Framework.** We analyze how each loss function contributes to the overall learning objective. We show the results of linear probing and fine-tuning accuracies on UCF101 and HMDB51

**Table 3: Ablation studies on the hyperparameters and key details. We report fine-tuning (ft) and linear probing (lin) accuracy on UCF101 split 1 unless otherwise specified. Default settings are colored in gray.****(a) Distance threshold  $\mathcal{T}$ .  $\mathcal{T} = 0.7$  yields better performance in general.**

threshold	ft	lin
0.35	82.6	71.9
0.7	83.1	73.1
1.4	83.4	71.0
2.8	80.6	69.8

**(d) Foreground ratio  $\beta$ . Small  $\beta$  is beneficial for the transferability of features**

ratio	ft	lin	ft <sub>h</sub>	lin <sub>h</sub>
0.3	82.2	71.6	56.0	41.2
0.5	83.1	73.1	54.2	39.2
0.7	81.9	71.5	54.3	39.0

**(b) Motion decoder depth. 2 blocks of decoder is the optimal setting.**

blocks	ft	lin
1	81.8	71.2
2	83.1	73.1
3	82.7	71.9

**(e) Foreground mask source. Using both modalities provides a more precise mask.**

source	ft	lin
RGB	81.6	72.1
frame difference	82.7	71.1
both	83.1	73.1

**(c) Decoder width and number of heads. Excess attention heads introduce noise.**

dim	nheads	ft	lin
256	4	82.7	73.3
	8	81.3	69.4
512	4	83.1	73.1
	8	81.7	71.6

**(f) Foreground mask position. Filtering out the noise on both sides is important.**

position	ft	lin
no mask	82.3	71.0
prediction side	81.8	71.7
target side	81.9	72.2
both	83.1	73.1

in Table 1. The vanilla instance-level video contrastive loss  $\mathcal{L}_{VV}$  serves as the baseline. We can observe that our pixel-level motion contrastive loss  $\mathcal{L}_{Pix}$  improves the baseline by a large margin and significantly outperforms the instance-level loss  $\mathcal{L}_{VD}$ . This observation verifies our idea of eliminating the weak alignment. The frame-level local motion loss  $\mathcal{L}_{Fra}$  also leads to notable performance gains. It is complementary to  $\mathcal{L}_{Pix}$  since it improves temporal diversity by aligning motion features at the frame level.

**Components of  $\mathcal{L}_{Pix}$ .** To eliminate the weak alignment of motion features, we propose a dense contrastive learning framework, foreground sampling strategy, and motion decoder in  $\mathcal{L}_{Pix}$ . We ablate the effectiveness of these components in Table 2. When only adopting the dense contrastive framework, the performances are compromised on the classification task [63]. The foreground sampling strategy and motion decoder can boost the performances independently or cooperatively by eliminating the spatial and temporal weak alignment. This also proves the existence of two kinds of weak alignment and the effectiveness of the proposed designs.

**Distance Threshold  $\mathcal{T}$ .** Table 3a ablates the distance threshold  $\mathcal{T}$  in dense contrastive learning framework. This parameter describes the range of motion features as the contrast target of a pixel.  $\mathcal{T} = 0.7$  yields better performance in general. The result is in accordance with the one in [64].

**Motion Decoder Design.** We first conduct experiments with different decoder depths in Table 3b. A 2-layer shallow motion decoder achieves the best results. More layers lead to a decrease in the results. We reason that more decoder layers may lead to overfitting of model training on the small-scale UCF101 dataset.

In Table 3c we ablate the decoder width and the number of heads. We observe that 8 attention heads decrease the performances. We argue that excess attention heads may sample information from some noisy latent subspaces. For the decoder width, considering that the motion decoder is also responsible for local motion reconstruction task, we use 512 dimensions by default. We provide more ablation studies in the supplementary material.

**Foreground Sampling Strategy.** We study the influence of the foreground ratio  $\beta$  in Table 3d. We additionally report the results

on HMDB51 in this study, noted as ft<sub>h</sub> and lin<sub>h</sub>. An intriguing observation is that  $\beta = 0.3$  obtains better results on HMDB51 and  $\beta = 0.5$  performs best on UCF101. We argue that aligning motion features with a small foreground ratio introduces the most relevant and noise-less motion information, which is critical for the transferability of the learned representations. On the other hand, a relatively large foreground ratio can provide more cues for instance discrimination but inevitably introduces more noise.

Table 3e studies the source of the foreground sampling mask. Using the combination of RGB and frame difference achieves the best results, as it locates the foreground region more precisely.

Table 3f studies the position of the foreground sampling mask. Applying a foreground mask on the prediction or target side means filtering out the background feature pixels in the corresponding feature map. We find background noise on either the prediction or the target side could damage the learned representations. Thus sampling foreground features on both sides is important.

### 4.3 Evaluation on Downstream Tasks

**Action Recognition on UCF101 and HMDB51.** We compare our method with the state-of-the-art self-supervised learning works on action recognition in Table 4. We report linear probing and fine-tuning Top-1 accuracy and list the detailed settings such as backbone architecture, number of frames, and resolution. For a fair comparison, we do not report methods using a deeper backbone or other modalities such as optical flow, audio, and text.

In linear probing settings, our method achieves the best results on both datasets. As the major counterparts with R(2+1)D backbone, DCLR [15] and SDC [43] also utilize frame difference as the source of motion information. FIMA outperforms DCLR and SDC in general, which implies we align the features of frame difference more precisely. With the I3D backbone pre-trained on Kinetics-400 for 100 epochs, our method consistently surpasses FAME [14] on both UCF101 and HMDB51, which is pre-trained for 200 epochs on Kinetics-400. It suggests that explicitly incorporating motion information is more effective than in an implicit manner.

**Table 4: Action recognition performance on UCF101 and HMDB51 under linear probing and fine-tuning settings. † denotes our reproduced results that strictly follow the settings in the original paper.**

Method	Backbone	Pretrain Dataset	Feames	Res	Linear		Finetune	
					UCF101	HMDB51	UCF101	HMDB51
VCP [36]	R3D-18	UCF101	16	112	-	-	66.3	32.2
PRP [66]	R(2+1)D	UCF101	16	112	-	-	72.1	35.0
DCLR [15]	R(2+1)D	UCF101	16	112	67.1	40.1	82.3	50.1
SDC [43]	R(2+1)D	UCF101	16	112	67.4	40.7	82.1	49.7
<b>FIMA(ours)</b>	R(2+1)D	UCF101	16	112	<b>71.2</b>	<b>41.1</b>	<b>84.1</b>	<b>56.0</b>
BE [55]	I3D	UCF101	16	224	-	-	82.4	52.9
FAME [14]	I3D	UCF101	16	224	67.2†	36.9†	81.2	52.6
<b>FIMA(ours)</b>	I3D	UCF101	16	224	<b>75.3</b>	<b>42.8</b>	<b>84.2</b>	<b>57.8</b>
CCL [30]	R3D-18	Kinetics-400	16	112	52.1	27.8	69.4	37.8
MemDPC [22]	R3D-34	Kinetics-400	40	224	54.1	30.5	78.1	41.2
RSPNet [9]	R(2+1)D	Kinetics-400	16	112	61.8	42.8	81.1	44.6
LSFD [4]	R3D-18	Kinetics-400	32	128	-	-	77.2	53.7
MLFO [44]	R3D-18	Kinetics-400	16	112	63.2	33.4	79.1	47.6
VideoMoCo [41]	R(2+1)D	Kinetics-400	32	112	-	-	78.7	49.2
TCLR [12]	R(2+1)D	Kinetics-400	16	112	-	-	84.3	54.2
DCLR [15]	R(2+1)D	Kinetics-400	16	112	72.3	<b>46.4</b>	83.3	52.7
FAME [14]	R(2+1)D	Kinetics-400	16	112	72.2	42.2	84.8	53.5
SDC [43]	R(2+1)D	Kinetics-400	16	112	72.1	45.9	86.1	54.8
<b>FIMA(ours)</b>	R(2+1)D	Kinetics-400	16	112	<b>73.1</b>	45.5	<b>86.7</b>	<b>59.4</b>
DSM [54]	I3D	Kinetics-400	16	224	-	-	74.8	52.5
BE [55]	I3D	Kinetics-400	16	224	-	-	86.8	55.4
FAME [14]	I3D	Kinetics-400	16	224	75.3†	46.7†	<b>88.6</b>	61.1
<b>FIMA(ours)</b>	I3D	Kinetics-400	16	224	<b>76.4</b>	<b>47.3</b>	88.5	<b>62.1</b>

**Table 5: Action recognition performance on Diving-48. All models are pre-trained on Kinetics-400.**

Method	Backbone	Res.	Finetune
TCLR [12]	R3D-18	112	22.9
BE [55]	I3D	224	62.4
FAME [14]	I3D	224	72.9
<b>FIMA(ours)</b>	R(2+1)D	112	<b>74.7</b>

In fine-tuning settings, our method with R(2+1)D obtains state-of-the-art results on both datasets. Remarkably, our R(2+1)D model pre-trained on UCF101 gets 56.0% classification accuracy on HMDB51, which outperforms all existing methods pre-trained on Kinetics-400. It demonstrates the data efficiency of our method and the high transferability of the learned representations. For the I3D network, FIMA pre-trained on UCF101 outperforms FAME by 3.0% and 5.2% on two datasets. When conducting pre-training on Kinetics-400, FIMA achieves competitive results with FAME with half training epochs (100 epochs vs. 200 epochs). Additionally, we report fine-tuning results on the less biased Diving-48 dataset [34] in Table 5. Our R(2+1)D pre-trained model with  $112 \times 112$  resolution outperforms previous methods with a larger backbone. It demonstrates that our method introduces truly aligned motion features and effectively suppresses background bias.

**Table 6: Recall-at-topK(%). Video retrieval performance under different K values on UCF101 and HMDB51. † denotes our reproduced results.**

Method	Backbone	UCF101				HMDB51			
		R@1	R@5	R@10	R@20	R@1	R@5	R@10	R@20
Pace [57]	R(2+1)D	25.6	42.7	51.3	61.3	12.9	31.6	43.2	58.0
MLFO [44]	R3D-18	39.6	57.6	69.2	78.0	18.8	39.2	51.0	63.7
CACL [20]	R(2+1)D	41.5	59.7	68.4	77.6	16.4	38.0	49.6	63.4
DCLR [15]	R(2+1)D	<b>54.8</b>	68.3	75.9	82.8	24.1	44.5	53.7	64.5
<b>FIMA(ours)</b>	R(2+1)D	52.2	<b>68.8</b>	<b>77.0</b>	<b>84.1</b>	<b>24.2</b>	<b>46.4</b>	<b>59.4</b>	<b>72.2</b>
DSM [54]	I3D	17.4	35.2	45.3	57.8	7.6	23.3	36.5	52.5
FAME† [14]	I3D	52.8	67.9	75.9	82.3	20.7	43.3	56.4	69.7
<b>FIMA(ours)</b>	I3D	<b>54.0</b>	<b>69.4</b>	<b>77.1</b>	<b>84.8</b>	<b>24.5</b>	<b>48.7</b>	<b>59.5</b>	<b>72.6</b>

**Video Retrieval.** We show the video retrieval performance on UCF101 and HMDB51 in Table 6. All models are pre-trained on UCF101 with a resolution of  $112 \times 112$  for R(2+1)D and  $224 \times 224$  for I3D. For R(2+1)D backbone, our method generally performs better than prior work DCLR [15] but slightly worse in the R@1 metric on UCF101. For the I3D backbone, FIMA achieves superior results on both datasets. The stable performance improvements with different network architectures demonstrate the effectiveness and strong generalization of our method.

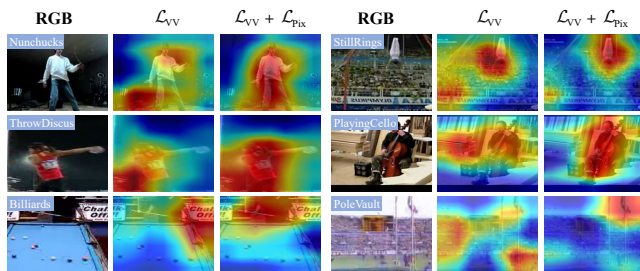


Figure 3: Class-agnostic activation map visualization for MoCo baseline (middle column) and MoCo+ $\mathcal{L}_{\text{PiX}}$  (right column).  $\mathcal{L}_{\text{PiX}}$  is effective for alleviating background bias.

#### 4.4 Visualization of Model Attention

To demonstrate the effectiveness of the proposed pixel-level motion contrastive loss  $\mathcal{L}_{\text{PiX}}$  for alleviating the background bias, we adopt the class-agnostic activation map [3] to visualize the model attention. The qualitative results of the I3D model are presented in Fig. 3. We can observe that the model pre-trained with the vanilla contrastive loss  $\mathcal{L}_{\text{VV}}$  severely suffers from background bias and falsely attends to static cues. Since  $\mathcal{L}_{\text{PiX}}$  introduces fine-grained motion information, the model pre-trained with  $\mathcal{L}_{\text{VV}} + \mathcal{L}_{\text{PiX}}$  correctly concentrates on the foreground area with significant motion.

#### 4.5 Why Is $\mathcal{L}_{\text{PiX}}$ More Effective?

To understand why is  $\mathcal{L}_{\text{PiX}}$  more effective than the vanilla motion contrastive loss  $\mathcal{L}_{\text{VD}}$ , we pre-trained the I3D network with  $\mathcal{L}_{\text{VV}} + \mathcal{L}_{\text{VD}}$  and  $\mathcal{L}_{\text{VV}} + \mathcal{L}_{\text{PiX}}$ , respectively. We visualize the class-agnostic activation maps in Fig. 4. It can be observed that the motion information introduced by  $\mathcal{L}_{\text{VD}}$  limited to the local area, while some significant motion cues are neglected. For example, in row-1 on the left, the ground-truth label is "BodyWeightSquats". The attention of the model trained with  $\mathcal{L}_{\text{VV}} + \mathcal{L}_{\text{VD}}$  concentrates on the upper part of the human body. However, the movement of the legs is critical to discriminate the "BodyWeightSquats" from other motions. On the contrary, the attention of the model trained with  $\mathcal{L}_{\text{VV}} + \mathcal{L}_{\text{PiX}}$  covers the whole foreground area, thus providing more comprehensive and holistic motion details for downstream tasks.

#### 4.6 Are Motion Features Well Aligned?

To verify whether the motion features are well aligned, we visualize the affinity matrices that describe the pairwise relationships between RGB and motion feature pixels. Specifically, we apply the average pooling to the extracted feature maps along the time dimension and then flat the output to the shape of  $49 \times 1024$ . Each pixel feature is normalized and the cosine similarity is used to calculate the relationship. The final matrix is averaged over 50 randomly selected video clips in the test set of UCF101. As shown in Fig. 5 (a), FIMA aligns the features of RGB and frame difference better in two aspects. First, the affinity matrix of FIMA has higher similarity around the diagonal. This indicates that every feature pixel learned by FIMA encodes more motion information around itself. Second, there are some outliers outside the diagonal in the affinity matrix of MoCo+ $\mathcal{L}_{\text{VD}}$ , while the affinity matrix of FIMA does not. This

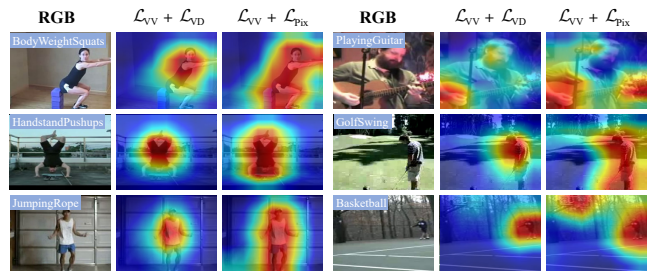


Figure 4: Class-agnostic activation map visualization for MoCo+ $\mathcal{L}_{\text{VD}}$  (middle column) and MoCo+ $\mathcal{L}_{\text{PiX}}$  (right column). Pre-training with  $\mathcal{L}_{\text{PiX}}$  provides richer motion information.

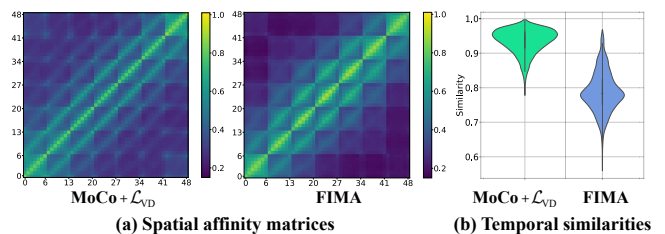


Figure 5: (a) Spatial affinity matrices and (b) Temporal similarity statistics between RGB features and motion features with MoCo+ $\mathcal{L}_{\text{VD}}$  pre-training and FIMA pre-training.

demonstrates that FIMA can retain spatial location information and facilitate a more accurate alignment of motion features. Besides, to demonstrate the effectiveness along the temporal dimension, we randomly select 50 videos in the test set of UCF101. For each video, we uniformly sample 10 clips and extract their pooled RGB and motion features. Then calculate the similarity of each pair of RGB and motion features. We visualize the similarities as a violin plot in Fig. 5 (b). We can observe that FIMA has a smaller mean similarity with a larger deviation, which indicates that the features learned by FIMA can better capture the variation of the motion semantics.

## 5 CONCLUSION

In this paper, we propose a novel self-supervised learning framework to incorporate well-aligned motion information. With the fine-grained motion supervision generated by the pixel-level contrastive learning paradigm, we eliminate the spatial and temporal weak alignments by designing a motion decoder and a foreground sampling strategy. Enabling a fine-grained spatiotemporal perception enhanced by accurate motion information. We achieve state-of-the-art results on standard benchmarks and extensive ablation studies demonstrate the effectiveness of our method.

## 6 ACKNOWLEDGMENTS

This paper is supported by the National Natural Science Foundation of China under Grants (62233013, 62073245, 62173248). Suzhou Key Industry Technological Innovation-Core Technology R&D Program (SGC2021035).



## REFERENCES

- [1] Humam Alwassel, Dhruv Mahajan, Bruno Korbar, Lorenzo Torresani, Bernard Ghanem, and Du Tran. 2020. Self-supervised learning by cross-modal audio-video clustering. In *Advances in Neural Information Processing Systems (NeurIPS)*, Vol. 33. 9758–9770.
- [2] Anurag Arnab, Mostafa Dehghani, Georg Heigold, Chen Sun, Mario Lúčić, and Cordelia Schmid. 2021. ViViT: A Video Vision Transformer. In *Proceedings of the IEEE/CVF International Conference on Computer Vision (ICCV)*. 6836–6846.
- [3] Kyungjune Baek, Minhyun Lee, and Hyunjung Shim. 2020. Psnynet: Self-supervised approach to object localization using point symmetric transformation. In *Proceedings of the AAAI Conference on Artificial Intelligence*, Vol. 34. 10451–10459.
- [4] Nadine Behrmann, Mohsen Fayyaz, Juergen Gall, and Mehdi Noroozi. 2021. Long Short View Feature Decomposition via Contrastive Video Representation Learning. In *Proceedings of the IEEE/CVF International Conference on Computer Vision (ICCV)*. 9244–9253.
- [5] Sagie Benaim, Ariel Ephrat, Oran Lang, Inbar Mosseri, William T. Freeman, Michael Rubinstein, Michal Irani, and Tali Dekel. 2020. SpeedNet: Learning the Speediness in Videos. In *Proceedings of the IEEE/CVF Conference on Computer Vision and Pattern Recognition (CVPR)*. 9922–9931.
- [6] Gedas Bertasius, Heng Wang, and Lorenzo Torresani. 2021. Is space-time attention all you need for video understanding?. In *International Conference on Machine Learning (ICML)*.
- [7] Tom Brown, Benjamin Mann, Nick Ryder, Melanie Subbiah, Jared D Kaplan, Prafulla Dhariwal, Arvind Neelakantan, Pranav Shyam, Girish Sastry, Amanda Askell, et al. 2020. Language models are few-shot learners. In *Advances in Neural Information Processing Systems (NeurIPS)*, Vol. 33. 1877–1901.
- [8] João Carreira and Andrew Zisserman. 2017. Quo Vadis, Action Recognition? A New Model and the Kinetics Dataset. In *Proceedings of the IEEE/CVF Conference on Computer Vision and Pattern Recognition (CVPR)*. 6299–6308.
- [9] Peihao Chen, Deng Huang, Dongliang He, Xiang Long, Runhao Zeng, Shilei Wen, Mingkui Tan, and Chuang Gan. 2021. Rspnet: Relative speed perception for unsupervised video representation learning. In *Proceedings of the AAAI Conference on Artificial Intelligence*, Vol. 35. 1045–1053.
- [10] Ting Chen, Simon Kornblith, Mohammad Norouzi, and Geoffrey Hinton. 2020. A simple framework for contrastive learning of visual representations. In *International Conference on Machine Learning (ICML)*. PMLR, 1597–1607.
- [11] Xinlei Chen, Haoqi Fan, Ross Girshick, and Kaiming He. 2020. Improved baselines with momentum contrastive learning. *arXiv preprint arXiv:2003.04297* (2020).
- [12] Ishan Dave, Rohit Gupta, Mamshad Nayem Rizve, and Mubarak Shah. 2022. Tclr: Temporal contrastive learning for video representation. *Computer Vision and Image Understanding* 219 (2022), 103406.
- [13] Jacob Devlin, Ming-Wei Chang, Kenton Lee, and Kristina Toutanova. 2019. Bert: Pre-training of deep bidirectional transformers for language understanding. In *NAACL*.
- [14] Shuangrui Ding, Maomao Li, Tianyu Yang, Rui Qian, Haohang Xu, Qingyi Chen, Jue Wang, and Hongkai Xiong. 2022. Motion-aware Contrastive Video Representation Learning via Foreground-background Merging. In *Proceedings of the IEEE/CVF Conference on Computer Vision and Pattern Recognition (CVPR)*. 9716–9726.
- [15] Shuangrui Ding, Rui Qian, and Hongkai Xiong. 2022. Dual contrastive learning for spatio-temporal representation. In *Proceedings of the 30th ACM International Conference on Multimedia*. 5649–5658.
- [16] Christoph Feichtenhofer, Haoqi Fan, Bo Xiong, Ross Girshick, and Kaiming He. 2021. A Large-Scale Study on Unsupervised Spatiotemporal Representation Learning. In *Proceedings of the IEEE/CVF Conference on Computer Vision and Pattern Recognition (CVPR)*. 3299–3309.
- [17] Chuang Gan, Boqing Gong, Kun Liu, Hao Su, and Leonidas J. Guibas. 2018. Geometry Guided Convolutional Neural Networks for Self-Supervised Video Representation Learning. In *Proceedings of the IEEE/CVF Conference on Computer Vision and Pattern Recognition (CVPR)*. 5589–5597.
- [18] Priya Goyal, Piotr Dollár, Ross Girshick, Pieter Noordhuis, Lukasz Wesolowski, Aapo Kyrola, Andrew Tulloch, Yangqing Jia, and Kaiming He. 2017. Accurate, large minibatch sgd: Training imagenet in 1 hour. *arXiv preprint arXiv:1706.02677* (2017).
- [19] Jean-Bastien Grill, Florian Strub, Florent Alché, Corentin Tallec, Pierre Richemond, Elena Buchatskaya, Carl Doersch, Bernardo Avila Pires, Zhaohan Guo, Mohammad Gheshlaghi Azar, et al. 2020. Bootstrap your own latent—a new approach to self-supervised learning. In *Advances in Neural Information Processing Systems (NeurIPS)*, Vol. 33. 21271–21284.
- [20] Sheng Guo, Zihua Xiong, Yujie Zhong, Limin Wang, Xiaobo Guo, Bing Han, and Weilin Huang. 2022. Cross-Architecture Self-supervised Video Representation Learning. In *Proceedings of the IEEE/CVF Conference on Computer Vision and Pattern Recognition (CVPR)*. 19270–19279.
- [21] Tengda Han, Weidi Xie, and Andrew Zisserman. 2019. Video Representation Learning by Dense Predictive Coding. In *Proceedings of the IEEE/CVF International Conference on Computer Vision Workshops (ICCVW)*.
- [22] Tengda Han, Weidi Xie, and Andrew Zisserman. 2020. Memory-augmented dense predictive coding for video representation learning. In *Proceedings of the European Conference on Computer Vision (ECCV)*. Springer, 312–329.
- [23] Kaiming He, Haoqi Fan, Yuxin Wu, Saining Xie, and Ross Girshick. 2020. Momentum Contrast for Unsupervised Visual Representation Learning. In *Proceedings of the IEEE/CVF Conference on Computer Vision and Pattern Recognition (CVPR)*. 9726–9735.
- [24] Deng Huang, Wenhao Wu, Weiwen Hu, Xu Liu, Dongliang He, Zhihua Wu, Xiangmiao Wu, Mingkui Tan, and Errui Ding. 2021. ASCNet: Self-supervised Video Representation Learning with Appearance-Speed Consistency. In *Proceedings of the IEEE/CVF International Conference on Computer Vision (ICCV)*. 8096–8105.
- [25] Lianghua Huang, Yu Liu, Bin Wang, Pan Pan, Yinghui Xu, and Rong Jin. 2021. Self-supervised Video Representation Learning by Context and Motion Decoupling. In *Proceedings of the IEEE/CVF Conference on Computer Vision and Pattern Recognition (CVPR)*. 13881–13890.
- [26] Simon Jenni, Givi Meishvili, and Paolo Favaro. 2020. Video representation learning by recognizing temporal transformations. In *Proceedings of the European Conference on Computer Vision (ECCV)*. Springer, 425–442.
- [27] Will Kay, Joao Carreira, Karen Simonyan, Brian Zhang, Chloe Hillier, Sudheendra Vijayanarasimhan, Fabio Viola, Tim Green, Trevor Back, Paul Natsev, et al. 2017. The kinetics human action video dataset. *arXiv preprint arXiv:1705.06950* (2017).
- [28] Salar Hosseini Khorasgani, Yuxuan Chen, and Florian Shkurti. 2022. SLIC: Self-Supervised Learning with Iterative Clustering for Human Action Videos. In *Proceedings of the IEEE/CVF Conference on Computer Vision and Pattern Recognition (CVPR)*. 16091–16101.
- [29] Dahun Kim, Donghyeon Cho, and In So Kweon. 2019. Self-supervised video representation learning with space-time cubic puzzles. In *Proceedings of the AAAI Conference on Artificial Intelligence*, Vol. 33. 8545–8552.
- [30] Quan Kong, Wenpeng Wei, Ziwei Deng, Tomoaki Yoshinaga, and Tomokazu Murakami. 2020. Cycle-contrast for self-supervised video representation learning. In *Advances in Neural Information Processing Systems (NeurIPS)*, Vol. 33. 8089–8100.
- [31] Haofei Kuang, Yi Zhu, Zhi Zhang, Xinyu Li, Joseph Tighe, Sören Schwaertfeger, Cyrill Stachniss, and Mu Li. 2021. Video contrastive learning with global context. In *Proceedings of the IEEE/CVF International Conference on Computer Vision (ICCV)*. 3195–3204.
- [32] H. Kuehne, H. Jhuang, E. Garrote, T. Poggio, and T. Serre. 2011. HMDB: A large video database for human motion recognition. In *Proceedings of the IEEE/CVF International Conference on Computer Vision (ICCV)*. 2556–2563.
- [33] Rui Li, Yiheng Zhang, Zhaofan Qiu, Ting Yao, Dong Liu, and Tao Mei. 2021. Motion-focused contrastive learning of video representations. In *Proceedings of the IEEE/CVF International Conference on Computer Vision (ICCV)*. 2105–2114.
- [34] Yingwei Li, Yi Li, and Nuno Vasconcelos. 2018. Resound: Towards action recognition without representation bias. In *Proceedings of the European Conference on Computer Vision (ECCV)*. Springer, 513–528.
- [35] Dezhao Luo, Chang Liu, Yu Zhou, Dongbao Yang, Can Ma, Qixiang Ye, and Weiping Wang. 2020. Video cloze procedure for self-supervised spatio-temporal learning. In *Proceedings of the AAAI Conference on Artificial Intelligence*, Vol. 34. 11701–11708.
- [36] Dezhao Luo, Chang Liu, Yu Zhou, Dongbao Yang, Can Ma, Qixiang Ye, and Weiping Wang. 2020. Video cloze procedure for self-supervised spatio-temporal learning. In *Proceedings of the AAAI Conference on Artificial Intelligence*, Vol. 34. 11701–11708.
- [37] Antoine Miech, Jean-Baptiste Alayrac, Lucas Smaira, Ivan Laptev, Josef Sivic, and Andrew Zisserman. 2020. End-to-end learning of visual representations from uncurated instructional videos. In *Proceedings of the IEEE/CVF Conference on Computer Vision and Pattern Recognition (CVPR)*. 9879–9889.
- [38] Ishan Misra, C Lawrence Zitnick, and Martial Hebert. 2016. Shuffle and learn: unsupervised learning using temporal order verification. In *Proceedings of the European Conference on Computer Vision (ECCV)*. Springer, 527–544.
- [39] Jingcheng Ni, Nan Zhou, Jie Qin, Qian Wu, Junqi Liu, Boxun Li, and Di Huang. 2022. Motion Sensitive Contrastive Learning for Self-supervised Video Representation. In *Proceedings of the European Conference on Computer Vision (ECCV)*. Springer, 457–474.
- [40] Aaron van den Oord, Yazhe Li, and Oriol Vinyals. 2018. Representation learning with contrastive predictive coding. *arXiv preprint arXiv:1807.03748* (2018).
- [41] Tian Pan, Yibing Song, Tianyu Yang, Wenhao Jiang, and Wei Liu. 2021. Video-MoCo: Contrastive Video Representation Learning with Temporally Adversarial Examples. In *Proceedings of the IEEE/CVF Conference on Computer Vision and Pattern Recognition (CVPR)*. 11205–11214.
- [42] Senthil Purushwalkam and Abhinav Gupta. 2020. Demystifying contrastive self-supervised learning: Invariances, augmentations and dataset biases. In *Advances in Neural Information Processing Systems (NeurIPS)*, Vol. 33. 3407–3418.
- [43] Rui Qian, Shuangrui Ding, Xian Liu, and Dahua Lin. 2022. Static and Dynamic Concepts for Self-supervised Video Representation Learning. In *Proceedings of the European Conference on Computer Vision (ECCV)*. Springer, 145–164.
- [44] Rui Qian, Yuxi Li, Huabin Liu, John See, Shuangrui Ding, Xian Liu, Dian Li, and Weiyao Lin. 2021. Enhancing Self-supervised Video Representation Learning via Multi-level Feature Optimization. In *Proceedings of the IEEE/CVF International*

- Conference on Computer Vision (ICCV)*. 7990–8001.
- [45] Rui Qian, Tianjian Meng, Boqing Gong, Ming-Hsuan Yang, Huisheng Wang, Serge Belongie, and Yin Cui. 2021. Spatiotemporal contrastive video representation learning. In *Proceedings of the IEEE/CVF Conference on Computer Vision and Pattern Recognition (CVPR)*. 6964–6974.
- [46] Alec Radford, Jong Wook Kim, Chris Hallacy, Aditya Ramesh, Gabriel Goh, Sandhini Agarwal, Girish Sastry, Amanda Askell, Pamela Mishkin, Jack Clark, et al. 2021. Learning transferable visual models from natural language supervision. In *International Conference on Machine Learning (ICML)*. PMLR, 8748–8763.
- [47] Adrià Recasens, Pauline Luc, Jean-Baptiste Alayrac, Luyu Wang, Florian Strub, Corentin Tallec, Mateusz Malinowski, Viorica Pătrăucean, Florent Altché, Michal Valko, Jean-Bastien Grill, Aäron van den Oord, and Andrew Zisserman. 2021. Broaden Your Views for Self-Supervised Video Learning. In *Proceedings of the IEEE/CVF International Conference on Computer Vision (ICCV)*. 1255–1265.
- [48] Khurram Soomro, Amir Roshan Zamir, and Mubarak Shah. 2012. UCF101: A dataset of 101 human actions classes from videos in the wild. *arXiv preprint arXiv:1212.0402* (2012).
- [49] Li Tao, Xueting Wang, and Toshihiko Yamasaki. 2020. Self-supervised video representation learning using inter-intra contrastive framework. In *Proceedings of the 28th ACM International Conference on Multimedia*. 2193–2201.
- [50] Li Tao, Xueting Wang, and Toshihiko Yamasaki. 2022. An improved inter-intra contrastive learning framework on self-supervised video representation. *IEEE Transactions on Circuits and Systems for Video Technology* 32, 8 (2022), 5266–5280.
- [51] Du Tran, Heng Wang, Lorenzo Torresani, Jamie Ray, Yann LeCun, and Manohar Paluri. 2018. A Closer Look at Spatiotemporal Convolutions for Action Recognition. In *Proceedings of the IEEE/CVF Conference on Computer Vision and Pattern Recognition (CVPR)*. 6450–6459.
- [52] Laurens Van Der Maaten. 2014. Accelerating t-SNE using tree-based algorithms. *The journal of machine learning research* 15, 1 (2014), 3221–3245.
- [53] Ashish Vaswani, Noam Shazeer, Niki Parmar, Jakob Uszkoreit, Llion Jones, Aidan N Gomez, Łukasz Kaiser, and Illia Polosukhin. 2017. Attention is all you need. In *Advances in Neural Information Processing Systems (NeurIPS)*, Vol. 30.
- [54] Jinpeng Wang, Yuting Gao, Ke Li, Jianguo Hu, Xinyang Jiang, Xiaowei Guo, Rongrong Ji, and Xing Sun. 2021. Enhancing unsupervised video representation learning by decoupling the scene and the motion. In *Proceedings of the AAAI Conference on Artificial Intelligence*, Vol. 35. 10129–10137.
- [55] Jinpeng Wang, Yuting Gao, Ke Li, Yiqi Lin, Andy J. Ma, Hao Cheng, Pai Peng, Feiyue Huang, Rongrong Ji, and Xing Sun. 2021. Removing the Background by Adding the Background: Towards Background Robust Self-supervised Video Representation Learning. In *Proceedings of the IEEE/CVF Conference on Computer Vision and Pattern Recognition (CVPR)*. 11804–11813.
- [56] Jiangliu Wang, Jianbo Jiao, Linchao Bao, Shengfeng He, Yunhui Liu, and Wei Liu. 2019. Self-Supervised Spatio-Temporal Representation Learning for Videos by Predicting Motion and Appearance Statistics. In *Proceedings of the IEEE/CVF Conference on Computer Vision and Pattern Recognition (CVPR)*. 4006–4015.
- [57] Jiangliu Wang, Jianbo Jiao, and Yun-Hui Liu. 2020. Self-supervised video representation learning by pace prediction. In *Proceedings of the European Conference on Computer Vision (ECCV)*. Springer, 504–521.
- [58] Xiaolong Wang, Ross Girshick, Abhinav Gupta, and Kaiming He. 2018. Non-local neural networks. In *Proceedings of the IEEE/CVF Conference on Computer Vision and Pattern Recognition (CVPR)*. 7794–7803.
- [59] Xinlong Wang, Rufeng Zhang, Chunhua Shen, Tao Kong, and Lei Li. 2021. Dense Contrastive Learning for Self-Supervised Visual Pre-Training. In *Proceedings of the IEEE/CVF Conference on Computer Vision and Pattern Recognition (CVPR)*. 3024–3033.
- [60] Donglai Wei, Joseph Lim, Andrew Zisserman, and William T Freeman. 2018. Learning and Using the Arrow of Time. In *Proceedings of the IEEE/CVF Conference on Computer Vision and Pattern Recognition (CVPR)*. 8052–8060.
- [61] Zhirong Wu, Yuanjun Xiong, Stella X. Yu, and Dahua Lin. 2018. Unsupervised Feature Learning via Non-parametric Instance Discrimination. In *Proceedings of the IEEE/CVF Conference on Computer Vision and Pattern Recognition (CVPR)*. 3733–3742.
- [62] Fanyi Xiao, Joseph Tighe, and Davide Modolo. 2022. MaCLR: Motion-Aware Contrastive Learning of Representations for Videos. In *Proceedings of the European Conference on Computer Vision (ECCV)*. Springer, 353–370.
- [63] Enze Xie, Jian Ding, Wenhai Wang, Xiahong Zhan, Hang Xu, Peize Sun, Zhenguo Li, and Ping Luo. 2021. DetCo: Unsupervised Contrastive Learning for Object Detection. In *Proceedings of the IEEE/CVF International Conference on Computer Vision (ICCV)*. 8392–8401.
- [64] Zhenda Xie, Yutong Lin, Zheng Zhang, Yue Cao, Stephen Lin, and Han Hu. 2021. Propagate Yourself: Exploring Pixel-Level Consistency for Unsupervised Visual Representation Learning. In *Proceedings of the IEEE/CVF Conference on Computer Vision and Pattern Recognition (CVPR)*. 16684–16693.
- [65] Dejing Xu, Jun Xiao, Zhou Zhao, Jian Shao, Di Xie, and Yueting Zhuang. 2019. Self-Supervised Spatiotemporal Learning via Video Clip Order Prediction. In *Proceedings of the IEEE/CVF Conference on Computer Vision and Pattern Recognition (CVPR)*. 10334–10343.
- [66] Yuan Yao, Chang Liu, Dezhao Luo, Yu Zhou, and Qixiang Ye. 2020. Video Playback Rate Perception for Self-Supervised Spatio-Temporal Representation Learning. In *Proceedings of the IEEE/CVF Conference on Computer Vision and Pattern Recognition (CVPR)*. 6548–6557.
- [67] Liangzhe Yuan, Rui Qian, Yin Cui, Boqing Gong, Florian Schroff, Ming-Hsuan Yang, Hartwig Adam, and Ting Liu. 2022. Contextualized Spatio-Temporal Contrastive Learning with Self-Supervision. In *Proceedings of the IEEE/CVF Conference on Computer Vision and Pattern Recognition (CVPR)*. 13977–13986.
- [68] Yujia Zhang, Lai-Man Po, Xuyuan Xu, Mengyang Liu, Yexin Wang, Weifeng Ou, Yuzhi Zhao, and Wing-Yin Yu. 2022. Contrastive spatio-temporal pretext learning for self-supervised video representation. In *Proceedings of the AAAI Conference on Artificial Intelligence*, Vol. 36. 3380–3389.
- [69] Bolei Zhou, Aditya Khosla, Agata Lapedriza, Aude Oliva, and Antonio Torralba. 2016. Learning deep features for discriminative localization. In *Proceedings of the IEEE/CVF Conference on Computer Vision and Pattern Recognition (CVPR)*. 2921–2929.

## A MORE IMPLEMENTATION DETAILS

### A.1 Technical Details.

For the details of MoCo-v2, we closely follow the settings in [11]. We use the symmetric loss [19] for optimization. The temperature parameter  $\tau$  is 0.1 for all losses, and the momentum parameter used to update the key encoder is 0.999. For  $\mathcal{L}_{VV}$  and  $\mathcal{L}_{Fra}$ , the size of the negative queue is 2048 for UCF101, and 65536 for Kinetics-400. The negative set  $\phi_n^k$  in  $\mathcal{L}_{Pix}$  is implemented as a queue with a size of 784 for UCF101 and 31360 for Kinetics-400. In particular, the negative pixels are from the dense feature maps in the same mini-batch when the pre-training is conducted on UCF101. (Note that in our case, the extracted motion feature map  $\tilde{M}^k \in \mathbb{R}^{2 \times 7 \times 7 \times C}$  and we set the size of mini-batch to 8).

### A.2 Motion Decoder Details.

Fig. 6 shows the architecture of the motion decoder. The first and the last linear layers are used to downsize and upscale the feature dimension. We apply a dropout of 0.1 in multi-head attention and feed-forward modules. We use simple 1D absolute positional encodings since it is enough to represent the spatial relations.

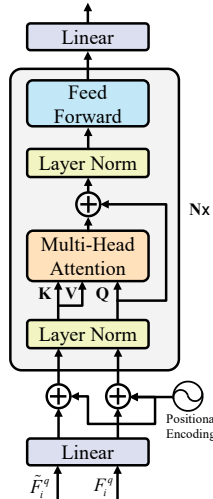


Figure 6: The architecture of the motion decoder.

### A.3 Self-supervised Pre-training Details.

All experiments are conducted on 3-8 NVIDIA RTX 2080 Ti GPUs, and RTX 3090 GPUs. We set mini-batch size of each GPU to 8. We use SGD optimizer with a momentum of 0.9 and a weight decay of  $10^{-4}$ . We randomly sample two 16-frame clips with a temporal stride of 2 at different timestamps and compute the frame difference, thus covering  $16 \times 2$  frames in total. For the frame-level motion reconstruction task, the 32 frames clip is divided into 2 sub-clips, each with 16 frames and a temporal stride of 1 and then compute the frame difference.

Following [14, 16], we use geometric data augmentation with RandomResizedCrop (scale  $\in [0.2, 1.0]$ ) and RandomHorizontalFlip (probability=0.5). For photometric augmentation, we adopt RandomGrayscale (probability=0.2), ColorJitter (probability=0.2), and

RandomGaussianBlur (probability=0.2, kernel\_size= 23 with standard deviation  $\in [0.1, 2.0]$ ).

### A.4 Details of Action Recognition.

In fine-tuning settings, we train for 150 epochs using the SGD optimizer with a momentum of 0.9 and a weight decay of  $10^{-4}$ . We set the initial learning rate to 0.0033 with a batch size of 16 and we decay the learning rate at epoch 60 and epoch 120 by a factor of 10. We use a dropout of 0.7 for UCF101 and 0.5 for HMDB51. Data augmentation is the same as in pre-training stage, except that RandomGaussianBlur is not applied.

In linear probing settings, we train for 100 epochs with an initial learning rate of 1.5 and a batch size of 16. The learning rate is decayed at epoch 60 and epoch 80 by a factor of 10. No dropout and weight decay is applied.

## B ADDITIONAL ABLATION STUDIES

We provide additional ablation studies in this section. The settings are the same as the main paper ablation studies.

### B.1 Decoder Width on All Losses.

In the main paper, we conduct ablations on the decoder width using  $\mathcal{L}_{VV}$  and  $\mathcal{L}_{Pix}$ . We provide an additional ablation in Table 7 using all losses:  $\mathcal{L}_{VV}$ ,  $\mathcal{L}_{Pix}$ , and  $\mathcal{L}_{Fra}$ .

When combined with the local motion reconstruction task, the decoder width of 256 dimensions is not capable enough to optimize both  $\mathcal{L}_{Pix}$  and  $\mathcal{L}_{Fra}$ , leading to a decrease in performance. Thus, we use 512 dimensions by default.

Table 7: Ablation study on the decoder width using  $\mathcal{L}_{VV}$ ,  $\mathcal{L}_{Pix}$ , and  $\mathcal{L}_{Fra}$ .

dim	ft	lin
256	82.5	72.3
512	<b>84.2</b>	<b>75.3</b>

### B.2 Effects of Using Shared Motion Decoders.

In our framework, we use the shared motion decoder to reduce the computational cost. In this way, two tasks can be accomplished in a single forward process, while using different decoders requires two forward processes and adds additional training parameters. Further, using the same decoder makes the optimization of two tasks more difficult, which potentially requires a higher quality of the features extracted by the encoder. To verify this, we perform an study as shown Table 8. Using a shared decoder achieves better results with fewer parameters.

Table 8: Ablation study on the shared or different motion decoder.

decoder	parameters	lin
shared	14.4M	<b>75.3</b>
different	16.5M	74.0

**Table 9: Ablation study on the various type of  $\mathcal{L}_{\text{Fra}}$ .**

loss types	lin
InfoNCE	<b>75.3</b>
Triplet	73.4
MSE	71.2

### B.3 Various Types of Frame-level Motion Loss.

The goal of the frame-level motion feature reconstruction is to enhance the temporal diversity of the learned features. By discriminating the positive sample from the intra-video negatives and inter-video negatives, the features extracted by the encoder become more discriminative along the temporal dimension (i.e. more time-aware). Thus, the introduction of negative samples is essential. Note that there are also other types of reconstruction losses such as Triplet Loss and MSE Loss. We perform an ablation study to explore their effects in Table 9. From the result, we can see that the InfoNCE loss performs best and MSE is the worst since no negative samples are introduced.

**Table 10: Ablation study on the number of negative samples in  $\mathcal{L}_{\text{Fra}}$ .**

losses	negative samples	lin
$\mathcal{L}_{\text{VD}}$	-	68.7
$\mathcal{L}_{\text{Pix}}$	98	70.3
$\mathcal{L}_{\text{Pix}}$	784	<b>73.1</b>
$\mathcal{L}_{\text{Pix}}$	1568	72.6

### B.4 The Number of Negative Samples in Pixel-level Motion Loss.

We perform an ablation study about the number of negative samples in  $\mathcal{L}_{\text{Pix}}$  as shown in Table 10. We set the number of negative samples to 98 (i.e. no motion features from other videos), 784 (i.e. motion features from the same mini-batch), and 1568 (i.e. use a queue to store motion features from other videos). We find that the introduction of motion pixel features from other videos facilitates a more accurate alignment of fine-grained motion features. Specifically, the introduction of the motion features from other videos boosts the performance, and the performance saturates after a certain number.

**Table 11: Ablation study on the training costs of  $\mathcal{L}_{\text{Pix}}$ . GPU-days is the number of GPUs used for pre-training multiplied by the training time in days.**

losses	DC	FS	MD	parameters	GPU-days	lin
$\mathcal{L}_{\text{VD}}$	-	-	-	12.3M	3.43	68.7
$\mathcal{L}_{\text{Pix}}$	✓	-	-	12.3M	3.53	69.7
$\mathcal{L}_{\text{Pix}}$	✓	✓	-	12.3M	3.54	71.2
$\mathcal{L}_{\text{Pix}}$	✓	✓	✓	14.4M	3.78	<b>73.1</b>

### B.5 Training Costs of Pixel-Level Motion Loss.

We report the actual pre-training time of our method with respect to the baseline as shown in Table 11. The wall-clock time of pre-training is benchmarked in 3 2080ti GPUs with a batch size of 24. Compared to  $\mathcal{L}_{\text{VD}}$ , we can see that the actual computational overhead added by the dense contrastive (DC) framework is marginal (+0.1 days). This is because most of the operations of the dense contrastive framework can be handled by efficient matrix multiplication in PyTorch. The motion decoder (MD) brings a +0.24 days training time increase due to the additional parameters.

## C LIMITATIONS AND FUTURE WORK.

Our method uses a non-parametric strategy and a fixed ratio  $\beta$  to sample the foreground pixels. Due to the strong bias of the model at the beginning of pre-training and the varying foreground ratio across videos, it inevitably omits useful information or introduces noise. Besides, our method originates from the dense contrastive learning framework. It is non-trivial to apply our method to dense predictive tasks in the video domain.

## D MORE VISUALIZATION ANALYSIS

### D.1 Point Attention of Motion Decoder.

In order to get a more intuitive understanding of how the motion decoder works, we visualize the point-attention map after pre-training in Fig. 7. For each source view, we first randomly pick one point (denoted by the red circle). Then, the RGB feature of this point and all features of the target view are input to the motion decoder. We visualize the attention score from the last layer of the motion decoder. The score is averaged over all attention heads.

As shown in Fig. 7, the motion decoder correctly matches the features of the person (row-1) and object (row-2), even with large variations in appearance. Further, with the input being background features, the motion decoder can also distinguish the background features in the target view (row-3). It coincides with our idea about avoiding the misalignment of background features by filtering out background features. In the last row on the left, it is interesting to see that the motion decoder can properly match features under strong occlusion. These observations suggest that the motion decoder builds an accurate and robust correspondence between the source view and the target view. These also demonstrate that the representations learned by FIMA have a clear distinction between different concepts in terms of person, object, and background.

### D.2 Foreground Sampling Mask.

We show the visualization of the foreground sampling mask in Fig. 8. We compute class-agnostic activation maps [3] of two modalities by applying the average pooling along channel and time dimensions. Then, we select patches with top- $[\beta HW]$  activation value as the foreground area. The foreground ratio  $\beta$  is set to 0.5. The black patches represent the filtered-out background. We find that either RGB or frame difference feature maps are likely to be disturbed by the background region. When one of the RGB masks and the frame difference masks deviates, the fused feature map always favors the correct one. This indicates that the strategy of using both RGB and frame difference to jointly determine the foreground features is working.

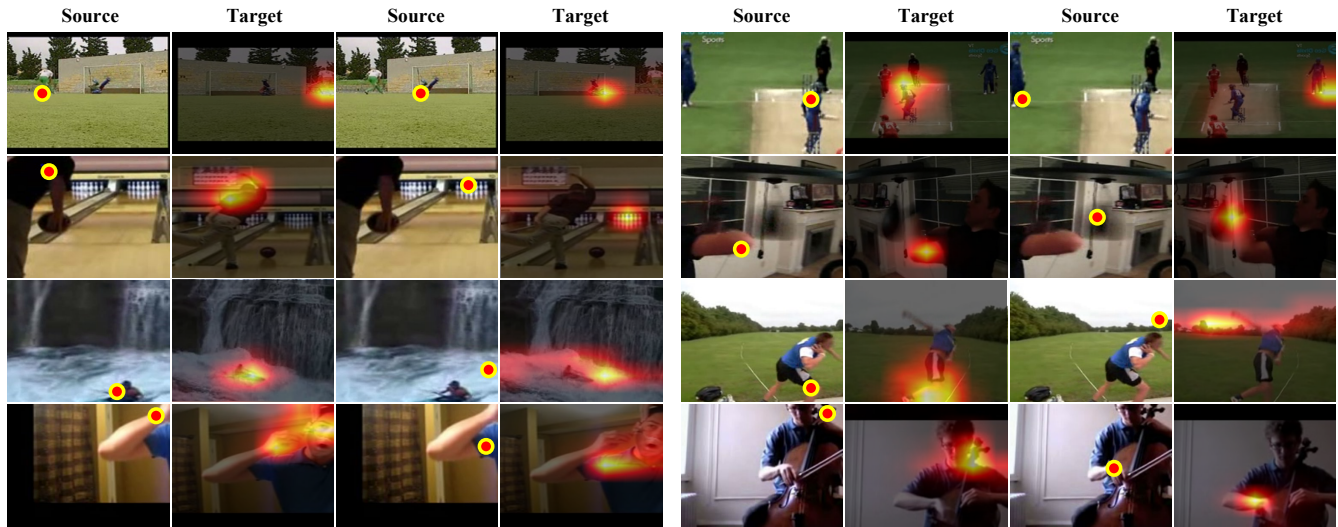


Figure 7: Point attention visualization of the motion decoder. In each group, we show the original source view with two selected points denoted by the red circle (column-1 and column-3), and their corresponding attention map from the last layer of the motion decoder in the target view (column-2 and column-4). Best viewed in color and zoomed in.

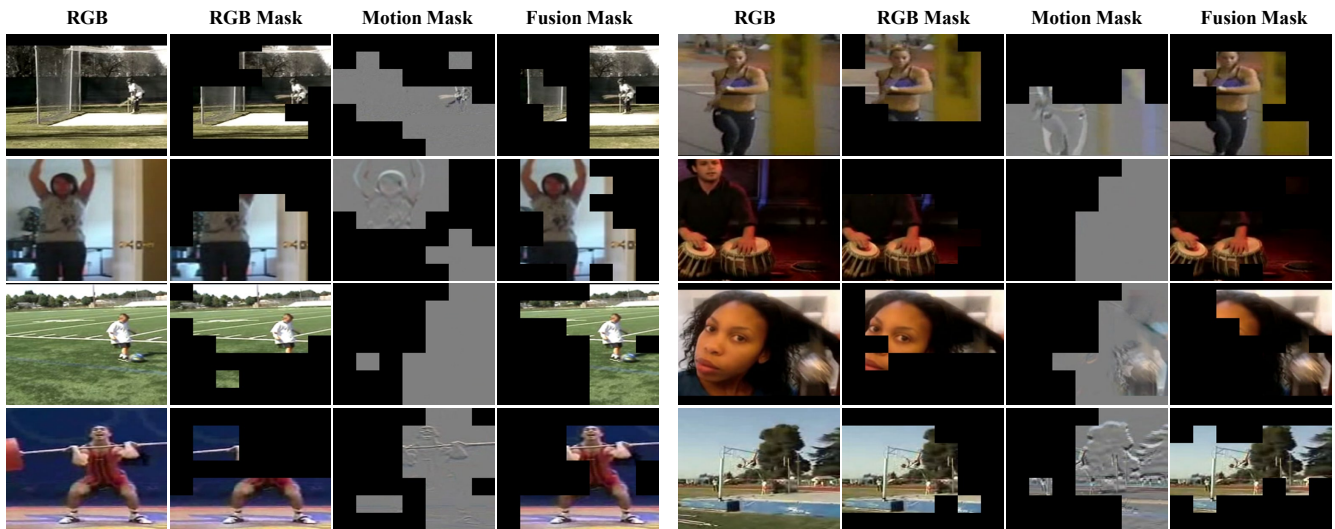


Figure 8: Visualization of the foreground sampling mask. In each group we show the RGB input (column-1), the foreground mask derived from the RGB feature map (column-2), the foreground mask derived from the frame difference feature map (column-3), and the fused foreground mask (column-4).

### D.3 Failure Cases of Foreground Sampling.

We show some failure cases of the foreground sampling mask in Fig. 9. When neither the RGB mask nor the frame difference mask focuses on the correct foreground region, the fused feature map also fails to locate the correct foreground area.

### D.4 Visualization of Learned Representations.

We use t-SNE [52] to visualize the representations learned by FIMA and MoCo baseline in Fig. 10 and Fig. 11. We pre-train the model on split 1 of UCF101 and visualize the representations of 20 randomly selected classes from the test set of UCF101. The perplexity for t-SNE is set to 30. From Fig. 10 and Fig. 11, we can observe that FIMA can facilitate the distribution of video representations in more discrete clusters.

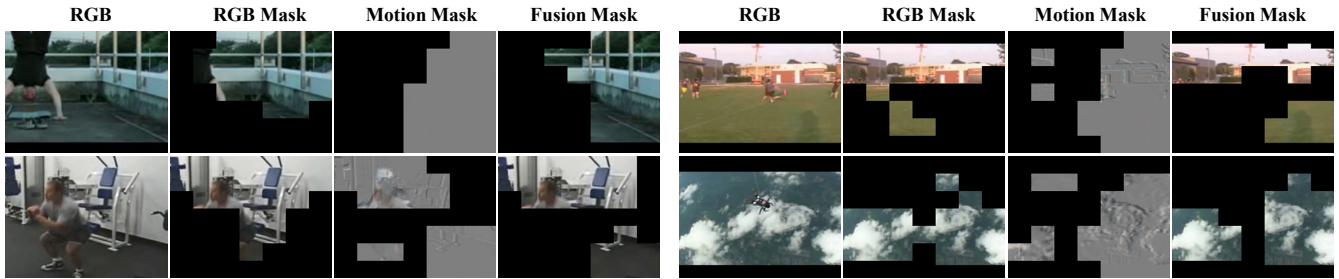


Figure 9: Failure cases of the foreground sampling mask.

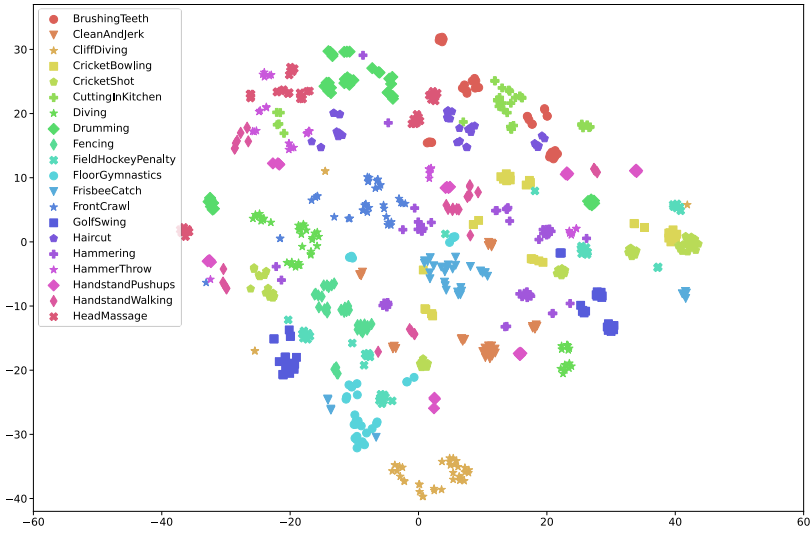


Figure 10: t-SNE visualization of FIMA representations for 20 randomly selected classes from the UCF101 test set.

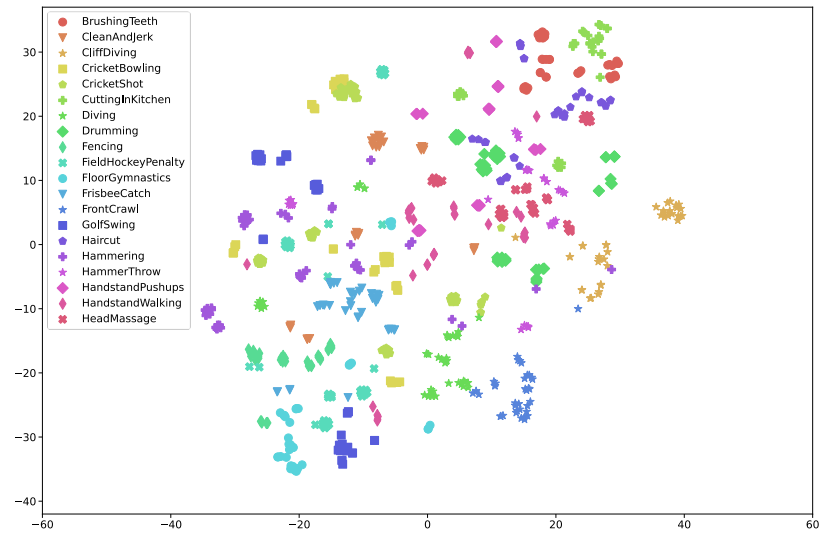


Figure 11: t-SNE visualization of MoCo representations for 20 randomly selected classes from the UCF101 test set.